Density Functional Theory Techniques for Electron Energy Loss Analysis of Lithium Materials

Quentin Stoyel, Mining and Materials Engineering, McGill University, Montreal

Month and Day of submission

A thesis submitted to McGill University in partial fulfillment of the requirements of the degree of Masters of Science

Abstract

A new method of calculating the magnitude of the core hole screening in the case of lithium materials is developed and implemented for the accurate simulation of Energy Loss Near Edge Structure (ELNES). ELNES is calculated for Li, Li_2O, and LiF with marked improvements in agreement between calculation and experiment, as well as superior quantitative and predictive abilities. The technique uses linear response theory to relate the electron density to the core hole shielding contribution from the valence electrons in a molecule. This contribution is then implemented via a non integer core hole in final state rule calculations. Abstract in French too

Acknowledgements

To all those useful folks

Contribution to Original Knowledge

A new method of investigating Lithium materials was developed. Density functional theory results are used to simulate Electron energy loss fine structure. The core hole approximation ex

Contents

Chapter 1

Introduction

The study of lithium materials has become increasingly relevant over the years. In particular, the field has been driven by the need to develop improved battery materials. This drive has come from an array of fields, amongst others, electric vehicles and portable electronics desiring longer lifetimes and faster charging. All aspects of batteries are currently being improved including capacity, charge density, and charge/discharge rates. As well as performance, other features such as safety and the ability to reuse or recycle battery materials are also growing fields.

In the realm of performance, lithium ion batteries offer a wide range of advantages. Lithium is the third element on the periodic table and consequently offers very high charge densities. This allows for batteries to become smaller and lighter without sacrificing lifetime. Additionally, lithium's lightweight nature make it highly mobile which is an attractive feature for increasing maximal discharge rate. Finally, as an alkali earth metal with a single weakly bound valence electron, lithium is highly electropositive which allows lithium ion batteries to achieve higher operating voltages than alternatives such as nickle-cadmium or lead-acid batteries. These potential performance advantages are illustrated in Fig 1.1.

The pursuit of developing new and improved battery materials has shifted the focus of analysis towards studying the microstructure of materials. The ability to identify crystal
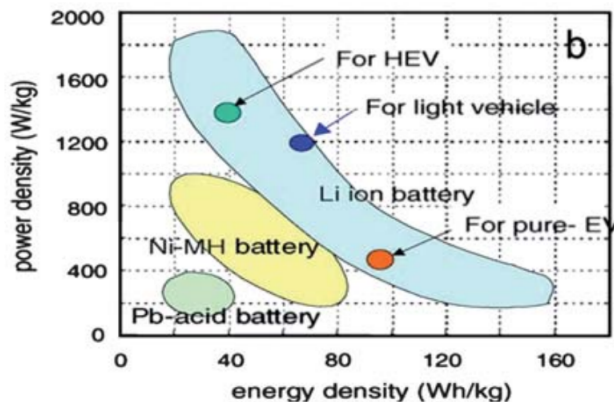
Figure 1.1: Plot illustrating the the power and energy densities achievable by three types of battery, as well as the minimum requirements for various types of electric vehicle, including hybrid electric vehicles (HEV), plug in hybrids (light vehicle). From [1]

structure and composition has become an essential element to understanding and tailoring material properties. On this front, electron microscopy has become a central technique to this effort [2]. Rapidly improving technology, the possibility of atomic level resolution, coupled with the increasing accessibility have made electron microscopy one of the most prevalent techniques for studying nanoscale features in materials. Here, however lithium is at odds with the method. Novel battery materials are increasingly intricate and lithium's lightness and easy to ionize nature make it particularly sensitive to electron beams, complicating analysis. Additionally, as the third element, it lies outside the ranges of many conventional theories. These properties make electron energy loss spectroscopy (EELS), a low dosage technique that is well suited for light elements such as lithium, attractive for battery material analysis [3]. However, EELS results have been historically qualitative and require strong theoretical support to be analyzed. The theoretical support is all the more essential in dealing with novel lithium materials that have limited sample life.

The theoretical support for EELS can come from a number of methods, however, the most prevalent of these are based in density functional theory (DFT), a first principles approach that requires only the locations of atoms in a crystal to determine material properties [4]. Here too, results have been limited to qualitative findings, further complicated by lithium's

lightweight nature which also poses challenges to theoretical approaches. The work performed in this thesis was to address some of the issues facing DFT methods concerning EELS of lithium. In particular, an improved method of calculating electron screening was implemented to improve the core hole approximation used to handle excitonic effects.

The outline of this thesis is as follows: in Chapter 2 we will begin with an overview of EELS, DFT and theoretical EELS calculations. Chapter 3 will describe the improved method developed in this work, and Chapter 4 will apply the method to a number of lithium materials. Chapter 5 will conclude the results and address future work.

Chapter 2

Literature Review

The focus of this work lies on theoretical calculations from first principles, designed to provide information on materials without the need for experiment. However, in order to verify new techniques, they must be confirmed with experiment. To this end, this chapter will commence with an overview of experimental electron microscopy and energy loss spectroscopy(EELS) before investigating how it is performed in the structure of density functional theory (DFT). We will conclude with a review of the various methods used to calculate EELS theoretically. The particularities of lithium materials will be discussed at each step of this process.

2.1 Electron Energy Loss Spectroscopy

2.1.1 Background

Materials are becoming increasingly refined with properties requiring characterization of nano scale features to unlock their full potentials [5]. At these length scales, even state of the art light microscopes lack the resolution to discern these features [6]. This limitation is due to the fact that nano scale features fall well below the diffraction limit of light microscopes [7]:

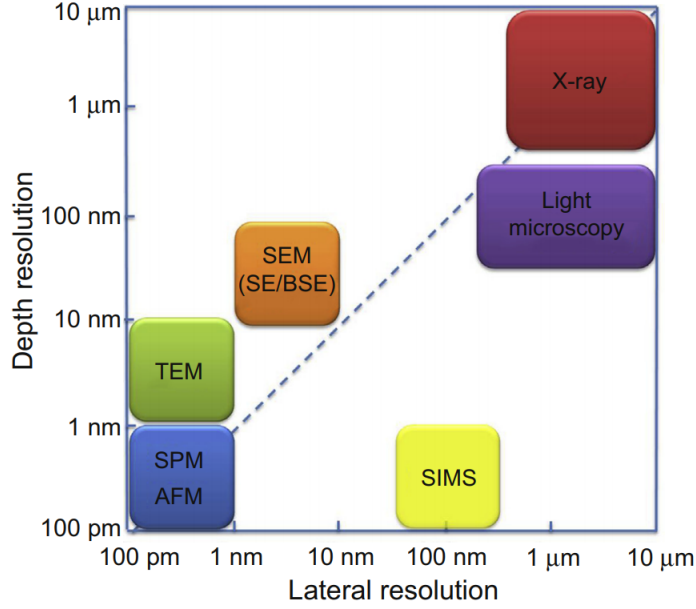$$d = \frac{\lambda}{2n \, \sin(\theta)} \tag{2.1}$$

Figure 2.1: Resolution achievable by various techniques including Transmission and Scanning electron microscopy (TEM/SEM) and light microscopy, on a log-log scale. Taken from Inkson, 2016 [2]

.

Where n is the refractive index and d is the smallest distance between 2 discernible objects. For optical light (λ = 400-800nm), it is impossible to routinely achieve the desired resolution ($\sim$ 1-50 nm) for characterization [6]. Electrons however have a wavelength dictated by [5]:

$$\lambda = \frac{h}{\sqrt{2m_0 eE}} \tag{2.2}$$

Where h is planck's constant, m_0, e and E are the rest mass, charge and energy of an electron. In an electron microscope, electrons are accelerated to energies on the order of 1-100 keV giving them wavelengths in the range from 1-100 pm (1pm = 10^{-12}m). Electron microscopes can therefore achieve a far lower theoretical diffraction limit and are currently limited by the technological constraints of the electron lenses [5]. Because of this high resolution, electron microscopes have become a key part of investigating material microstructure [2]. This dramatic increase in resolution compared to alternative methods is illustrated in Fig 2.1.

Incident Beam

Auger Electrons

X Rays

Secondary Electrons

Backscattered Electrons

Visible Light

Specimen

Absorbed Electrons

Electron Hole Pairs

Interaction Volume

Elastically Scattered Electrons
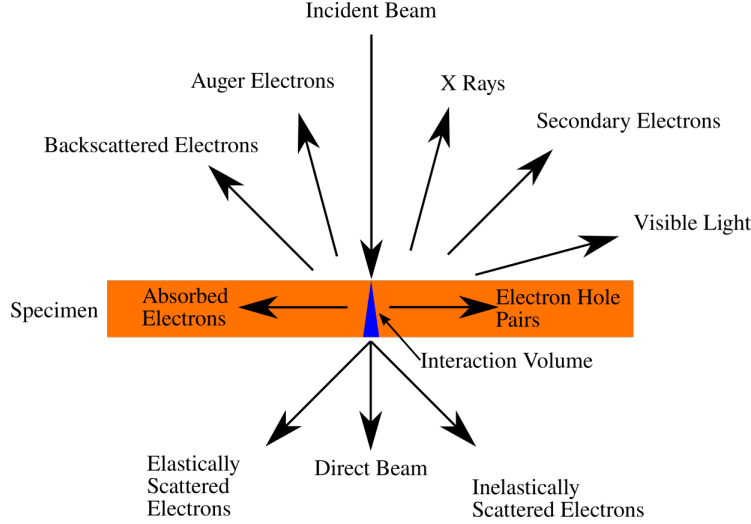
Direct Beam

Inelastically Scattered Electrons

Figure 2.2: The numerous types of signals emitted when an electron beam encounters a sample in a TEM/STEM. Redrawn from Williams and Carter [8].

In addition to the ability to image samples with high resolution, electron microscopy generates a large number of different and useful signals which can be used for both to characterize samples as well as imaging them, see Fig 2.2 [8]. A full discussion of the various techniques electron microscopes used to investigate each of these accessible signal types is beyond the scope of this work and has been well documented elsewhere [3; 5; 8; 9]. Instead, we will focus on the relevant technique, electron energy loss spectroscopy (EELS). EELS is an electron microscopy technique that analyzes the transmitted inelastically scattered electrons, Fig 2.2[3]. It is mainly an analytic technique, however it is also possible to perform imaging with EELS [10]. EELS consists of collecting electrons that have passed entirely through the sample and binning them according to how much energy each one has lost, resulting in a spectrum such as in Fig 2.3. The mechanism of energy loss for the beam electrons is by exciting the samples electrons in a number of ways, which is reflected by the multiple different features in the spectrum [3]. The main features in EELS spectra are:

- **Zero Loss Peak:** The majority of the electrons in EELS pass through the specimen without experiencing an inelastic interaction, and retain their initial energy. The width of this peak defines the resolution of the spectrum and is due to energy spreading as
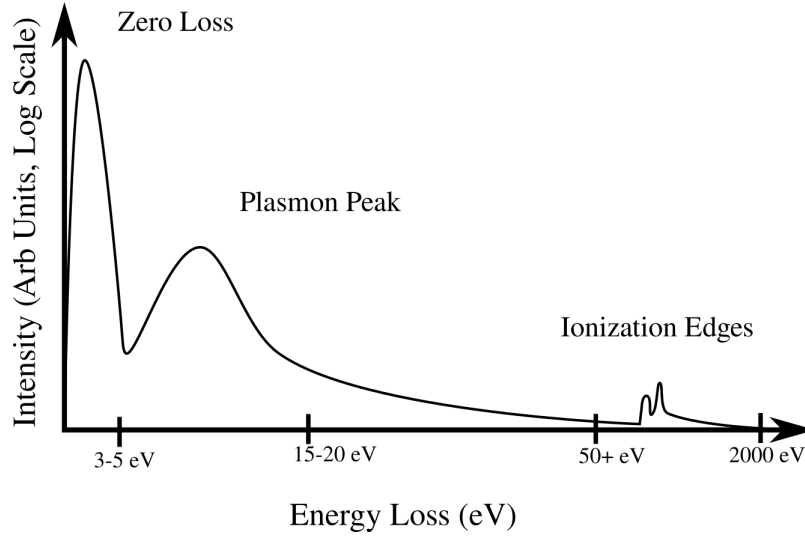
Figure 2.3: Sample EELS spectra identifying the main features, the zero loss peak, plasmon peak and ionization edges wwith fine structure. The intensities are on a log scale, and span approximately 6 orders of magnitude between the zero loss and the ionization edges.

the beam passes through the electron lenses [11]. For thin samples, zero loss peak is also the most intense feature on a spectrum [3].

- **Plasmon Peak:** The electron beam can excite multiple atoms in the solid collectively, creating a wavelike oscillation in electron cloud of the solid [3]. These ae called plasmon excitations and result in a peak appearing between 5-30eV [3]. The shape and intensity of the peak is dependent on the bond strength in the material and can be used to probe properties such as thickness and surface topology [12; 13].

- **Ionization Edges:** Beam electrons can also excite core electrons in the sample to the conduction band. As an atom's core states are in general isolated from its surroundings, the "edges" for each element will occur at specific energy locations, independent of sample, analogous to characteristic x-rays [3]. These can be used to determine sample composition [3].

- **Background:** Beam electrons can excite loosely bound electrons close to the Fermi level into the unoccupied conduction band. Due to the large number of possible transi-
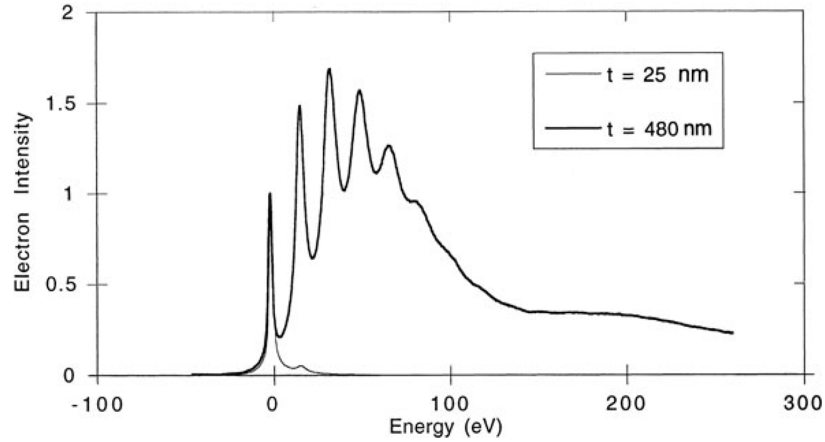
Figure 2.4: Two spectra demonstrating the importance of thin samples and single scattering events. In the thicker sample, the majority of beam electrons experience one or multiple plasmon excitations, resulting in multiple evenly spaced plasmon peaks with larger intensity than the zero loss. The higher background from the plasmon peaks and the thicker sample drown out any structure due to ionization edges [3]. Image taken from Egerton, 2011 [3]

tions and the fact that high energy events are less favourable, this results in a smoothly decaying background [3].

Another key factor that needs consideration, is that in order for meaningful data to be extracted from a spectra, the number of electrons that experience multiple inelastic events must be minimized [3]. If not, duplicate plasmon peaks will appear in the spectra, and because of their relatively high intensity, the weaker ionization edges will become drowned out by the background, see Fig 2.4. As well, any electron that experiences an ionization event will likely also experience some form of plasmon interaction, further smearing any ionization edges in thicker samples.

Near Edge Structure

Unlike x-ray edges in EDS which have distinct, simple shapes, higher energy resolution in EELS reveals additional features in the ionization edges extending up 50 eV beyond the onset of the edge [3]. These features are a reflection of the unoccupied states in the conduction
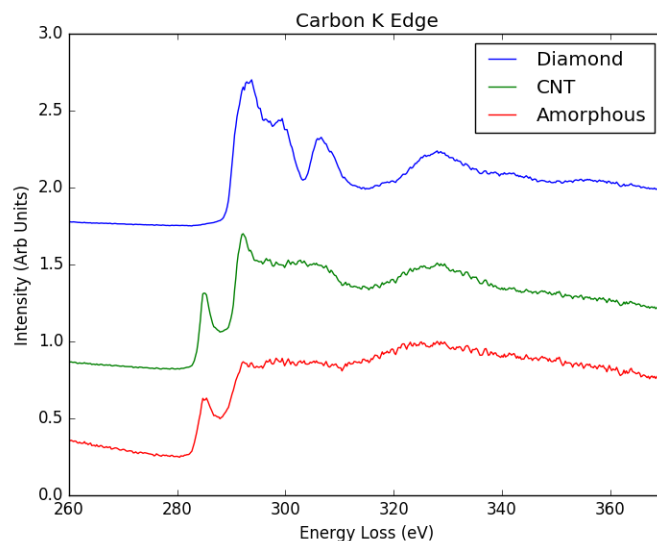
8

Figure 2.5: Carbon K edge taken at 30keV at McGill. The different crystal structures (amorphous, diamond and carbon nanotube) result in distinctly different ELNES which can be used for identification.

band that represent the final states of sample electrons excited by the beam. The band structure of the conduction band is largely dependent on the local bonds of the atom in question. Because of this, ELNES can be used to investigate the local environment of each element. This can be used to distinguish different crystal structures of the same element such as carbon in graphite vs diamond, see Fig 2.5 [14]. ELNES is also sensitive to impurities that would effect the band structure.

2.1.2 EELS in Experiment

In order to collect EELS spectra, electrons must pass entirely through the sample, making EELS a technique for transmission electron microscopes (TEM's) or scanning transmission electron microscopes (STEM) technique [3]. The main features of the two techniques are illustrated in Fig ??? but a more in depth discussioncan be found in Goldstein, William and Carter, and Egerton [3; 5; 8] In order to collect these transmitted electrons, a magnetic field prism is placed below the specimen and redirects the electrons into a detector, Fig FIG!.

9
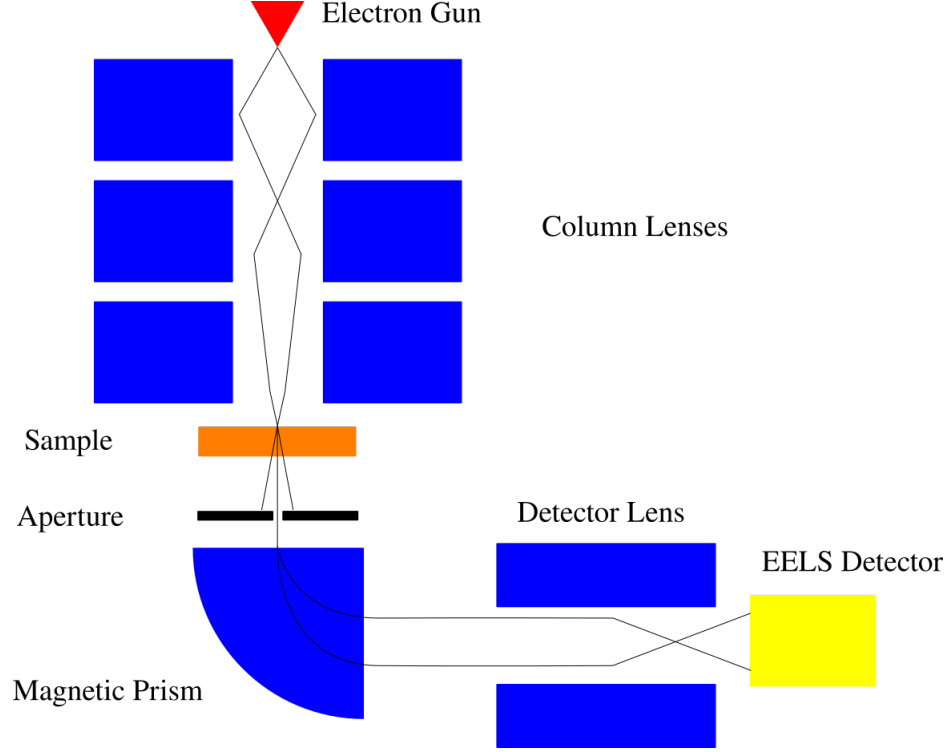
Figure 2.6: Experimental EELS setup, with the various magnetic lenses depicted in blue.

Inside the magnetic prism, there is a $\tilde{B}$ field perpendicular to the beam direction and the transmitted electrons are exposed to a Lorentz force:

$$\vec{F_B} = q(\vec{v} \times \vec{B}) \tag{2.3}$$

As the force varies according to the velocity of the electrons, the magnetic prism also separates the electrons according to their energy:

$$\vec{F_B} = e(\vec{v} \times \vec{B}) = \frac{m\vec{v}^2}{\vec{r}} = \vec{F_c} \tag{2.4}$$

$$r = \frac{mv}{eB} = \frac{\sqrt{2mE}}{eB} \tag{2.5}$$

Where e is the charge of an electron and E is the energy of each electron after passing through the sample. By mapping each location on the detector to a corresponding energy loss value the final spectra are obtained.

TEM vs STEM

There are two distinct types of electron microscope that can before EELS, TEM and STEM, each with their own advantages. TEM's operate between 100-300 keV in parallel beam conditions, allowing for thicker samples and better resolution. STEM's operate in the 30 keV range and offer the ability for EELS imaging as well as being considerably more economical than TEM's. A summary of EELS in each of these techniques is presented in Table TABLE!.

Lithium in EELS

Lithium materials present a number of challenges to EELS analysis. As the lightest alkali metal it is almost always ionized and highly mobile. Additionally, lithium ion battery materials are in general insulators with band gaps of varying sizes. These features make lithium materials highly sensitive to electron beam damage. When the electron beam pass through a sample, it results in charge build up. In electron conductive samples (eg. metals), this charge can be dissipated to a certain extent, however in materials with a band gap (eg. insulators, battery cathodes), this charge can displace the charged and mobile lithium ions and break down the crystal structure. Lithium's high mobility also make them vulnerable to knock on damage. This effect occurs when an electron interacts inelastically with an atom's nucleus and transfers sufficient energy to it to displace it from its lattice site. Lithium is particularly vulnerable to this interaction because its high mobility, meaning that it requires only a small amount of energy to displace it through a crystal. Lithium's only ionization edge is its K-edge is located at ∼55eV, at the boundary of what is considered reasonable for analysis. The low edge places it close to the plasmon decay complicating background subtraction. This energy range also often results in overlap between the lithium K-edge and the $M_{2/3}$ and M_4 edges of transition metals. In particular the edges of Mn, Fe and Ni, all fall between 40-70eV. As these elements are key components to cathode materials, they can require further steps for analysis to be possible.

2.1.3   Preprocessing

There are two key steps to be performed upon acquiring an ELNES spectra before it can be used for meaningful conclusions, background subtraction and deconvolution.

Background Subtraction

The smooth decaying background in EELS spectra needs to be removed in order for meaningful comparison and measurements to be made on ELNES. However, the EELS background does not decay at a fixed rate and changes based on the presence of edges and with energy [15]. Consequently, it is not currently possible to fit remove a single function to an entire spectrum. Instead, the method of choice relies on fitting to a window directly before an ionization edge and refitting for each edge as needed. The most prevalent function used for this purpose is a power law decay [3]:

$$I_{bg} = AE^{-r} \tag{2.6}$$

Where E is the energy loss and A and r are fitting factors. This method has limitations due to different regions of the spectra decaying at different rates, in particular, for the plasmon peak, r $\sim$ 4-5? yet at higher energies ($\geq$100eV) r $\sim$ 3?. A downside of this method is the final results dependence on the size and location of the fitting window on the final output, see Fig FIG. This instability has resulted in a number of alternate models being proposed for specific cases, however, the power law method remains the most prevalent.

Deconvolution

Despite drastic improvements, there is still a degree of energy spread on beam electrons, typically in the range of $\sim$0.5-3eV. This energy spread results in the observed ELNES on a spectra to be a result of a convolution between the 'actual' ELNES and the zero loss peak. Additionally, the probability of an electron undergoing plural scattering (scattering inelastically more than once in the specimen) must also be accounted for, as the low loss

region of the spectrum is also convoluted into the output spectra. Plural scattering can best be seen in thicker samples where it results in the presence of multiple plasmon peaks, although it is present on the entire spectrum. In order to recover the single scattering spectrum, the output must undergo deconvolution. A number of techniques exist for this purpose. Fourier techniques rely on describing the signal as a number of convolutions:

$$J(E) = Z(E)) * [\delta(E) + \frac{S(E)}{I_0} + \frac{S(E) * S(E)}{2!I_0} + ...]$$ (2.7)

Where J(E) is the obtained spectra, Z(E) is the zero loss peak, S(E) is the single scattering spectra, and I_0 is the integrated intensity of the zero loss. The double scattering term is the convolution of the two single scattering terms, weighted by the decreased probability according to Poisson statistics. Taking a Fourier transform of this turns all of the convolutions into products:

$$j(\nu) = z(\nu)(1 + \frac{s(\nu)}{I_0} + \frac{s^2(\nu)}{2!I_0} + \frac{s^3(\nu)}{3!I_0})...$$ (2.8)

Which can in turn be collapsed into an exponential:

$$j(\nu) = z(\nu)\exp[s(\nu)/I_0]$$ (2.9)

This equation can then be solved for $s(\nu)$ and reverse Fourier transformed to obtain the single scattering spectra. In order to avoid amplifying the noise in the original spectra, which is represented by high frequency terms in Fourier space, the result must be broadened by a modifier to minimize these terms. Thus, deconvolution can only improve the energy resolution of a spectra to a certain extent.

More recently, Bayesian methods have found success as well, in particular the Richardson-Lucy technique [16]. This technique is based on iterative methods initially developed in astronomy and used for the deconvolution of images, including some from the Hubble space telescope [17]. From the same starting point, the convolution of the ideal spectra with the low loss, or point spread function:

$$J(E) = R(E) * S(E) \tag{2.10}$$

As an EELS spectra is inherently pixilated by the CCD, at each pixel we can apply Poisson statistics to define the probability of obtaining the observed number of counts (N) [16]:

$$P(N/N_m) = \frac{e^{-N_m} N_m^N}{N!} \tag{2.11}$$

By iteratively varying N_m and maximizing the probability, the deconvoluted spectra can be obtained. Similar to Fourier methods however, the noise on the spectra increases with more iterations, in order to conserve information.

2.1.4 A Note on Other Experimental Techniques

EELS is by no means the only experimental technique available for the analysis of material microstructure, nor is it even the only electron microscopy technique available for the task. Other prevalent techniques include x-ray based analysis such as x ray absorption spectroscopy and energy dispersive spectroscopy. We will take a moment to briefly describe these methods.

X Ray Absorption Spectroscopy (XAS)

XAS operates on a similar principle to EELS. Instead of probing the sample with an electron probe, a beam of x-rays is directed through the sample and the resulting energy losses in the output spectrum are binned as in EELS [18]. The difference in probe media does not effect the measured quantity which is the same as in EELS: the unoccupied density of states of the material [18]. Because of their similarities, parallels are often drawn between EELS and XAS when developing theories. The largest benefit of XAS is it's superior energy resolution ($\sim$0.1 eV) when compared to EELS ($\sim$1 eV) allowing for more features in near edge structures to be identified[3; 18]. This benefit comes at a cost however, XAS needs to be performed in a synchrotron, making it far more costly and less accessible to perform than EELS

Energy Dispersive Spectroscopy (EDS)

EDS is another form of analytic spectroscopy performed in electron microscopy. Unlike EELS and XAS which measure the unoccupied density of states, EDS measures the occupied DOS [5]. Like EELS, EDS probes the sample with an electron beam, but then collects the emitted x-rays produced when the sample electrons return to their relaxed states following excitation. These x-rays have the same characteristic energies as in EELS, but EDS lacks the resolution to distinguish fine structure. As such, it is limited to providing composition information on samples. EDS is however less strict on sample requirements as it does not require the thin samples needed by EELS and can therefore be used to analyze both bulk and microscale features in samples [5].

2.1.5 Lithium in EELS

The focus of this work lies in application to lithium materials and a brief discussion of their experimental nature is in order. Lithium's lightweight, easily ionizable nature that make it ideal for battery applications come at the cost of making lithium remarkably sensitive to an electron beam. The highly energized charged beam of electrons used to analyze sample in a SEM/TEM inflicts a range of damage onto lithium samples including evaporation of lithium and collapse of crystal structures. As such minimizing beam exposure is essential to performing measurements on lithium materials. EELS is an effective means of reaching this target, as it is possible to obtain signal from the majority of ionization events and requires only a few seconds to obtain. However, in EELS lithium presents a new challenge, the only ionization edge lies at ~ 55 eV close to the background tail of the plasmon peak. As a result, lithium EELS specimens must be made thin enough to minimize plural plasmon scattering or risk drowning out the relatively weak lithium k-edge features.

A second range of features of lithium are its minimal interactions with x-rays. As such a light element, lithium has a low fluorescence yield, producing a single x-ray per 10,000 ionization events. Additionally, lithium's low Z number also results in a minimal cross

section relative to interact with x-rays. Consequently, lithium is essentially invisible to x-ray diffraction (XRD) techniques, and can only be detected on the most sensitive electron dispersive spectroscopy (EDS) systems.

These various features highlight impressive technological advances that have been necessary to even study lithium experimentally on this size scale. They also demonstrate the need for strong theoretical support to interpret novel lithium results obtained in challenging situations.

2.2   Density Functional Theory

Many of the results from EELS have non-intuitive interpretations, particularly in the case of ELNES which relies largely on qualitative comparisons between measured and database spectra. Consequently, new materials and situations require a degree of theoretical support to analyze novel results. This support often comes from ab initio calculations, amongst other density functional theory (DFT). This section will describe the basis of DFT and how it can be used to calculate EELS, in particular in the context of lithium, as well as looking into other theoretical techniques to support EELS.

2.2.1   Background

DFT is an ab initio method that requires only atomic positions as input. By solving a modified version of the Schrodinger equation, it is possible to obtain the ground state energy of the system, and from there determine a range of other properties, including ELNES. This almost direct treatment of quantum mechanics make DFT one of the most accurate techniques, however, the quadratic to cubic scaling of the method limit its applicability to small scale systems, Fig 2.7. DFT's success and flexibility have resulted in the development of a large number (90+) of codes, both open source and commercial, and its place in a wide array of fields.
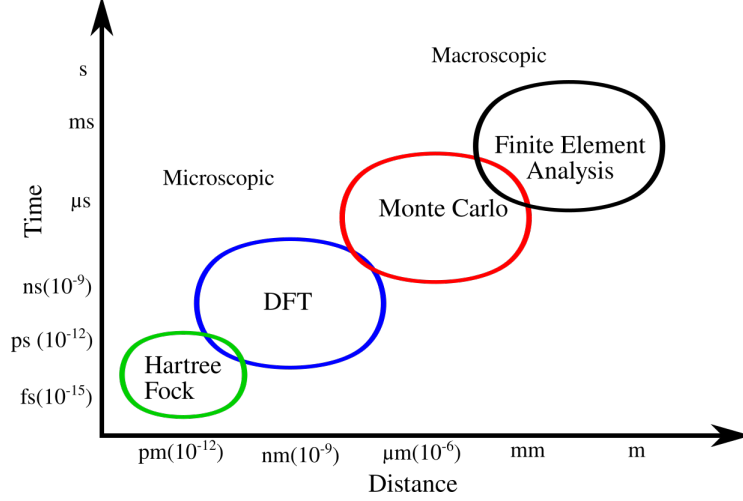
Figure 2.7: Various methods available to compute material properties and their correspond-
ing regions of use.

2.2.2 Formulation

DFT relies on solving the multi-bodied form of the Schrodinger equation [19]. Our aim is to
obtain a solution for ψ from which observable properties can be calculated.

$$\frac{-\hbar^2}{2} \sum_i^N \frac{\nabla^2 \psi_i}{m_i} + \sum_i^N V(\mathbf{r}_i)\psi_i = E\psi \tag{2.12}$$

In this case, we will consider the non-relativistic, spin independent, time independent
case, although more in-depth derivations can be found elsewhere [20]. We will now perform
the Born Oppenheimer approximation, and assume that the nuclei can be separated from the
electrons and will act classically. This is a safe assumption, as the mass difference between
nuclei and electron is by more than a factor of 1000 [21]:

$$\left[\frac{-\hbar^2}{2m_e} \sum_i^N \nabla^2 + \sum_i^N V(\mathbf{r}_i) + \sum_i^N \sum_{j<i} U(\mathbf{r}_i, \mathbf{r}_j) \right] \psi_i(\mathbf{r}_i) = E\psi_i \tag{2.13}$$

Where m_e is the mass of an electron, N is the number of electrons, and $\mathbf{r}_i$ is a position
vector. The terms inside the square brackets are collectively know as the Hamiltonian and
are, respectively, the kinetic energy of all the electrons, the Coulomb interaction between
the electrons and the collective nuclei, and the Coulomb reaction between the electrons [19].

17

At this point, this equation is still too unwieldy to solve, it depends on 3N variables (the position coordinates of each wavefunction), not to mention the many body problem lurking inside the double sum. Facing this conundrum, we take advantage of the Hohenberg-Kohn Theorems which postulates [22]:

- The ground state *energy* of the system is a unique functional of the ground state *electron density.*

- The electron density that minimizes the overall energy corresponds to the real ground state density.

By changing the variables being solved for to the *density* and not wavefunctions, we can simplify the problem down to only three variables: the three coordinates of the density field. The Hohenberg-Kohn theorems indicate that we can make everything a functional of electron density and that any density other than the groundstate will result in a higher energy in the system [23]. We now define the term functional, as an object that acts like a function, except takes other functions as input instead of variables, eg:

$$F[f(x)] = f(x)^2 \tag{2.14}$$

In the case at hand, the relevant functional is the energy which is a functional of the density: $E[n(\mathbf{r})]$. From the Hohenberg-Kohn theorems, we can begin working towards a more manageable equation for energy. We continue by further breaking down the potentials and writing them in terms of density as needed:

$$\left[-\frac{\hbar}{2m_e} \sum_i \int \psi_i^* \nabla^2 \psi_i d^3r + \int V(\mathbf{r}) n(\mathbf{r}) d^3r + \frac{e^2}{2} \int \int \frac{n(\mathbf{r})n(\mathbf{r}')}{|r - r'|} d^3r d^3r' + E_{\text{nuclei}} + E_{\text{XC}} \right] [\psi_i] = E[\psi_i] \tag{2.15}$$

Where the first term is the kinetic energy of the electrons, the second is the energy from the electron density-nuclei interaction with $V(\mathbf{r})$ is the electric field created by the nuclei; the third term is the electron density-electron density Coulomb interaction and E_{nuclei} is the contribution from nucleus-nucleus interaction. The final term, E_{XC} is the exchange and

correlation term and is where all of the quantum features of the electrons have been grouped; the price to pay for substituting in density. This equation cannot be directly solved from first principles by itself, we need some way to obtain the electron density. On this front we introduce the Kohn -Sham equations which assume that we can decouple all of the electrons into single particle equations:

$$\left[T_i + V(\mathbf{r}) + V_{\mathrm{H}}(\mathbf{r}) + V_{\mathrm{XC}}(\mathbf{r})\right]\phi_i(\mathbf{r}) = \epsilon_i\phi_i(\mathbf{r}) \tag{2.16}$$

Where ϕ_i and ϵ_i are the Kohn sham wavefunctions and eigenvalues respectively and V_H is the Hartree potential or:

$$V_{\mathrm{H}} = e^2 \int \frac{n(\mathbf{r'})}{|r - r'|}d^3r' \tag{2.17}$$

Which represents the interaction of the electron in question (the one at r, not r') and all the electrons in the sample. This results in some interaction between the electron and itself, a term that must be corrected for in the V_{XC} term. The Kohn-Sham equations can be readily solved, but require the density to calculate the Hartree potential. The density is in turn given from the wavefunctions:

$$n_{\mathrm{KS}}(\mathbf{r}) = 2\sum_i \phi_i^*\phi_i \tag{2.18}$$

Where the 2 is to account for electron spin. As the density is needed to calculate the wavefunctions and vice versa, a self consistent approach must be taken in order to obtain a valid result:

1. Assume a starting density

2. Use the initial density to calculate the Hartree potential and use it to solve the Kohn-Sham equations for the wavefunctions

3. Calculate a new density using Eqn. 2.18.

4. Compare the new density to the initial, update the initial density.

5. Repeat steps 2-4 until the density converges and the energy is minimized. This density then represents the groundstate for the system.

This method is the starting point for DFT calculations, from here there are a number of different variations with regards how to go about these steps. Amongst others, the treatment of the exchange-correlation potential and choice of basis for the wavefunctions is what separates the methods.

Exchange-Correlation Potential

The exchange-correlation potential was introduced above, but not defined. That is because there no easily solvable form for this term as it must collect all of the unknown features not accounted for in the rest of the Kohn-Sham equations, ie electron's being indistinguishable, the self interaction term, etc. There have been a number of proposed potentials, many designed for specific situations. Like the other potentials in the KS equations, the XC potential is defined as a functional of density. The various potentials vary according to accuracy and computational cost. The first attempt, originally proposed by Kohn and Sham in 1965 was the local density approximation (LDA) in which the XC potential depends only on the density [4; 24]:

$$E_{\text{XC}}[n(\mathbf{r})] = \int n(\mathbf{r})\epsilon_{\text{XC}}[n(\mathbf{r})]d^3r \qquad (2.19)$$

LDA is exact in the case of a free electron gas and has obtained good success when applied to metallic solids. By considering the gradient of the density as well, a more involved potential is obtained, called the generalized gradient approximation (GGA) [24; 25] :

$$E_{\text{XC}}[n(\mathbf{r})] = \int n(\mathbf{r})\epsilon_{\text{XC}}[n(\mathbf{r}), \nabla n[\mathbf{r}]]d^3r \qquad (2.20)$$

Other parameters can also be taken into consideration, such as the potential energy (meta GGA)or empirical factors (hybrid functionals) [24; 26]. Depending on the desired property and available computing power, an appropriate functional should be chosen for each case.

Basis Sets

A second defining feature for DFT is the choice of basis set for the wavefunctions, ϕ_i, and a number of options have become prevalent in the available programs. These are divided into two distinct types, localized and periodic [19]. Localized basis sets rely on using orthogonal functions decay rapidly away from the origin [19]. An example is Gaussian peaks, as is used in the Gaussian16 software package [27]. The very localized basis set is useful for handling single, isolated molecules, and as such is ideally suited applications in quantum chemistry and biology. The ability to handle isolated cases limits the maximal size of system that can be studied. In materials science, a typical system of interest is a crystallographic material and to handle these cases, periodic basis sets are used. By defining a unit cell and repeating it infinitely in all directions, we obtain a periodic potential. The solution to the Schrödinger equation under these boundary conditions is given by Bloch waves, defined as [28]:

$$\psi = u(\mathbf{r})e^{i\cdot\mathbf{k}} \tag{2.21}$$

Consequently, a natural basis choice for periodic boundary situations are plane waves, which are used in popular DFT packages including VASP, Quantum Espresso and Wien2k [29–31]. The periodic boundary method allows for accurate calculation of in theory infinite samples representative of bulk materials. Computation limits still apply to the size of the unit cell, typically limited to at most a few hundred atoms. This effect renders features such as defects and grain boundaries quite expensive as they must be contained in a cell large enough to isolate them from their images in adjacent cells. As large numbers of plane waves would be required to handle the fine features in the electron density close to nuclei, often an augmented plane wave (APW) technique is used. APW lowers the computational cost by dividing the unit cell into two regions: interstitial space and atomic basins, illustrated in Fig 2.8 [31].

The ability to divide electrons into two groups is due to the fact that the core electrons surrounding each atom are largely unaffected by their local environment as they are screened by the outer shells [31]. The choice of which basis set is used inside the muffin tins provides
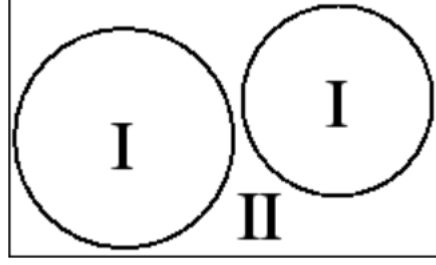
Figure 2.8: The two regions in an APW approach. (I) Atomic Basins modelled with Psu-dopotentials or atomic orbitals and (II) interstitial space modelled with a plane wave basis set [31].

further options between DFT codes. One option is pseudopotentials, which are pre-generated densities for each element, which can be varied to match the plane waves at the boundary. The pseudopotential method is used in a number of codes, amongst others, VASP and QE [29; 30]. Alternatively, spherical harmonics which correspond to the atomic orbitals can be used for increased accuracy [28]. This type of DFT is referred to as all-electron or full potential, as every electron is represented in the basis set, unlike the PP method where many are absorbed into the pre-calculated PP [31]. Fitting for all of the electrons in the sample comes at a computational cost, yet allows for more accurate analysis of properties dependent on core states.

A flowchart demonstrating the various properties of DFT codes is presented in Fig 2.9

2.2.3 WIEN2k

WIEN2k is the DFT code used for the majority of this work. It uses a linearized augmented plane wave (LAPW) formulation, combining plane waves with spherical harmonics as in Fig 2.8 [31]. It is an all electron code requiring only an input crystal structure, essential for handling the necessary core states in EELS calculations [31]. In WIEN2k's standard formalism, the basis sets for the Kohn-Sham wavefunctions can be represented as:
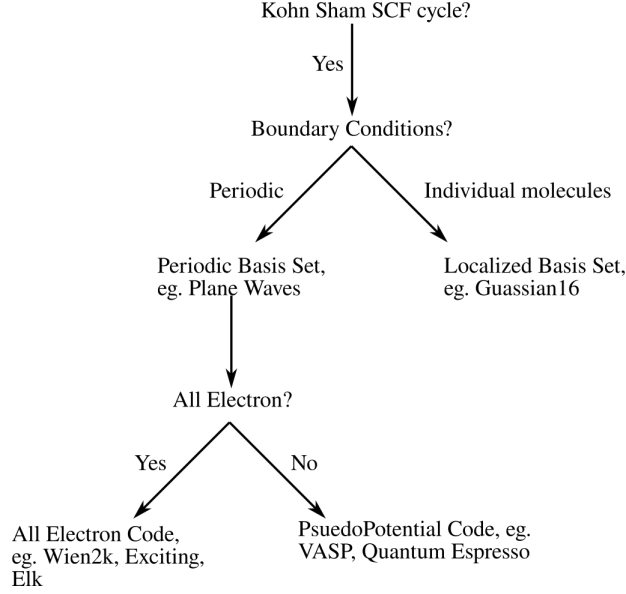
Figure 2.9: Flowchart depicting the various choices of basis set available to DFT codes.

$$\phi_{k_n} = \begin{cases} \Sigma_{lm}[A_{lm,\mathbf{k}_n}u_l(r,E_l) + B_{lm,\mathbf{k}_n}\dot{u}_l(r,E_l)]Y_{lm}(\hat{\mathbf{r}}) & r \leq r_{\mathrm{RMT}} \\ \frac{1}{\sqrt{\omega}}e^{i\mathbf{k}_n\cdot\mathbf{r}} & r > r_{\mathrm{RMT}} \end{cases} \quad (2.22)$$

Where $Y_{lm}(\hat{\mathbf{r}})$ are the spherical harmonics and $u_l(r,E_l)$ are the solutions to the radial Schrödinger equation. The coefficients $A_{lm,\mathbf{k}_n}$ and $B_{lm,\mathbf{k}_n}$ are set so as to match the value and slope of the plane waves at the boundary. This standard method can be further augmented by the addition of local orbitals (LAPW + lo). These are used to help account for so called semi core states

2.2.4   Lithium in DFT

As in experiment, lithium's low atomic number presents a range of difficulties in DFT. These are largely due to loosely bound electrons with large orbitals resulting from lithium's small nuclear charge. As a result, even the 1s level electrons in lithium can have orbitals extending well past 2.5 Bohr from the nuclei, far further than in larger elements, see Fig 2.10 [32]. This results in a number of issues. Firstly, it is difficult and sometimes impossible to set the atomic spheres large enough to contain all these 1s core electrons. As atomic spheres
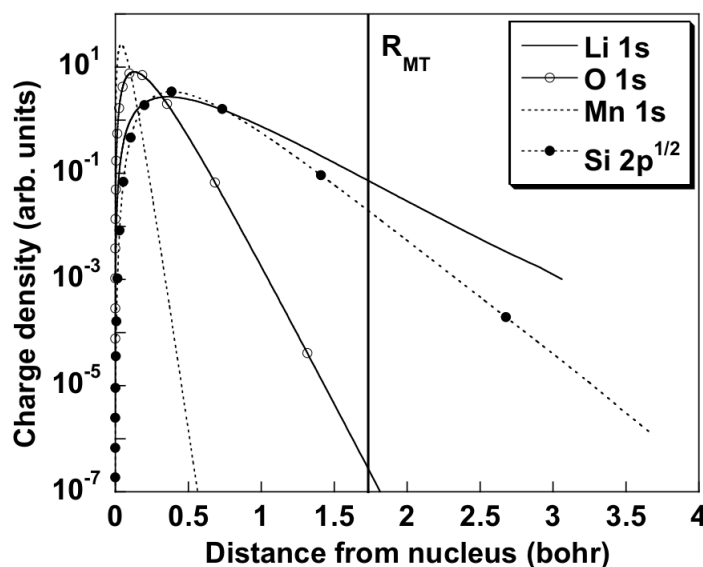
Figure 2.10: Orbital charge densities as a function of distance from nucleus, demonstrating the varying degrees of localization. From Mauchamp et al [32]

cannot overlap, they are typically limited to $\sim$ 2.0 Bohr. Depending on the compound, the sphere size can be further constrained as all the spheres must be roughly the same size (within 30%) [31]. If the sphere sizes are too varied, convergence time and accuracy can deteriorate dramatically. The alternative to large sphere size is to allow a degree ($\sim$0.5%)of core leakage into the calculation [31]. The downside to allowing leakage is that it may result in non physical effects at later stages in the calculation, or result in the appearance of "ghostbands" in the calculation [31].

Quantum Theory of Atoms in Molecules

One of the properties that can be calculated through DFT is the electron density and how this relates to atomic bonds. Work on analyzing the density and defining bonds and atomic basins was performed by Bader [33]. The cloud of electrons associated with each atom is delimited by a surface satisfying [34]:
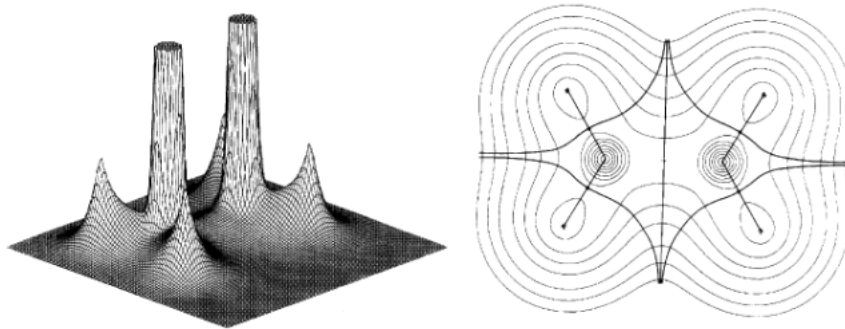
Figure 2.11: Density plot (left) and identification of atomic basin (right) in diborane atomic
From Bader [33].

$$\nabla \rho(\mathbf{r}) \cdot \mathbf{n}(\mathbf{r}) = 0 \qquad \forall \mathbf{r} \in S(\Omega, \mathbf{r}) \tag{2.23}$$

That is the surface with no flux of electron density through it and can be pictured as a
"valley" in the electron density "landscape," see Fig 2.11. In order to calculate the location
of these surfaces, critical points in the density field are located, defined when $\nabla \rho(\mathbf{r}) = 0$, and
always satisfy Eq. 2.23. With the exception of critical points at maximas in $\rho(\mathbf{r})$ which are
located at nuclei, all of the critical points lie on interatomic surfaces[35]. By evaluating the
nature of the critical point (minima, first or second order saddle point) the location of bonds
in the material can be located as well, centred on first order saddle point critical points [35].

2.3 EELS Calculations

Having described the inner workings of DFT, we will now investigate how we can use the
ground state density, Kohn-sham wavefunctions and eigenvalues to calculate the features of
an EELS spectra. DFT is however a ground state theory; the Hohenberg Kohn theorems
only guarantee that agreement between the calculation and reality for the lowest energy
state. As EELS inherently involves exciting an atom above this ground state, a number
of assumptions must be made to address this issue. The various approaches to the issue
of handling excitations are defining features of many of the techniques used to calculate

EELS. Additionally, the varying requirements to handle the wide array of features in EELS spectra further diversify the techniques. Broadly there are three methods for calculating EELS, multiple scattering, atomic multiplet and band structure methods. We will discuss a number of the band structure methods as well as their advantages and applicability below.

2.3.1 Time Dependent Density Functional Theory -TDDFT

There are a number of ways to approach the problem of calculating EELS spectra [36; 37]. In TDDFT, the ELNES is computed through the macroscopic dielectric function (ϵ_M). As is the case with many ELNES calculations, we begin from Fermi's Golden Rule, which determines the probability of an electron being driven to a new state by some propagator:

$$M_{nm\mathbf{k}} = \langle n\mathbf{k}|e^{-i(\mathbf{q}+\mathbf{G})\mathbf{r}}|n'\mathbf{k}+\mathbf{q}\rangle \tag{2.24}$$

Where $\mathbf{q}$ is the momentum transfer from the beam to the sample and $\mathbf{G}$ is the Fourier coefficient of the probe. The initial and final states are the key parameters taken from DFT. These matrix elements can be used to determine the independent particle polarizability χ^{KS} [38]:

$$\chi^{KS}_{\mathbf{G},\mathbf{G}'}(\mathbf{q},\omega) = \frac{1}{V}\sum_{nm\mathbf{k}}\frac{f_{n\mathbf{k}} - f_{m\mathbf{k}+\mathbf{q}}}{\epsilon_{n\mathbf{k}} - \epsilon_{m\mathbf{k}+\mathbf{q}} + \omega + i\delta}M_{nm\mathbf{k}}(\mathbf{q},\mathbf{G})M^*_{nm\mathbf{k}}(\mathbf{q},\mathbf{G}') \tag{2.25}$$

Where $f_{n\mathbf{k}}$ is the fermi distribution. χ^{KS} can be related to the reducible polarizability through the Dyson equation:

$$\chi = \chi_{KS} + \chi_{KS}(\nu + f_{xc})\chi \tag{2.26}$$

Where f_{xc} is the exchange and correlation potential. A common approximation is to set this to zero, a method called the Random Phase Approximation (RPA) [36]. At this point we make two more approximations. We first assume a that $\mathbf{q} \to 0$, referred to as the optical limit. This assumes that the momentum transfer to the sample is minimal, an approach that is valid for low energy losses (<50eV). We also assume that the probe wavelength is much

larger than the resulting perturbations, thus ($\mathbf{G} \rightarrow 0$). This is know as ignoring local field effects. Both of these approximations can be relaxed on a case by case basis, however this comes at increased computational cost [38]. With these approximations, we can proceed to calculate first element of the dielectric tensor:

$$\epsilon_{00}^{-1}(\mathbf{q}, \omega) = 1 + v\chi \tag{2.27}$$

from which we can calculate the macroscopic dielectric function which relates to the energy loss function:

$$[\epsilon_{\mathrm{M}}(\mathbf{q}\omega)]^{-1} = \epsilon_{00}^{-1}(\mathbf{q}, \omega) \tag{2.28}$$

$$L(\mathbf{q}, \omega) = -\mathrm{Im}[\epsilon_{\mathrm{M}}(\mathbf{q}, \omega)]^{-1} \tag{2.29}$$

The energy loss function is what is directly measured by EELS and is the standard of comparison to TDDFT. TDDFT is accurate for low losses, so ideal for calculations of plasmons, and in the limit of the optical approximation low energy M edges of transition metals, and notably the lithium K edge. Limitations of the approach are that it is based on the final state rule, and thus is susceptible to excitonic effects in $\langle f|$. Additionally, local field effects can be subtle and come at computational cost to include [39]. TDDFT is also applicable to x-ray absorption spectroscopy where the optical limit is more valid. The only required modifications to the theory are a modification to the propogator in Eq. 2.24.

2.3.2 Cross Section Approach

TDDFT is a suitable choice for low loss EELS. For higher energy ionization edges with non-negligible momentum transfer, Fermi's Golden Rule can be used to compute a double differential cross section instead of the dielectric function. The differentials are with respect to energy and scattering angle, the two relevant parameters in an EELS experiment. The relationship is given by [40]:

$$\frac{\partial^2 \sigma}{\partial \Omega \partial E} = \left[\frac{4\gamma^2}{a_0{}^2 q^4} \right] \frac{k_f}{k_i} \sum_{i,f} |\langle f|e^{i\mathbf{q}\cdot\mathbf{r}}|i\rangle|^2 \delta(E - E_f + E_i) \tag{2.30}$$

Where a_0 is the Bohr radius, E the energy loss and $\gamma = \sqrt{1 - \beta^2}$, the relativistic factor. As in TDDFT, the approach can be modified to solve for XAS, by replacing the Rutherford cross section with the Thompson cross section in the prefactor and changing the propagator from [41]:

$$e^{i\mathbf{q}\cdot\mathbf{r}} \rightarrow e^{i\mathbf{k}\cdot\mathbf{r}} \epsilon \cdot \mathbf{r} \tag{2.31}$$

The cross section formalism can also be modified to account for anisotropic samples as well as some experimental parameters [40]. Similar to TDDFT, the essential parameters are the initial and final states, taken from DFT ($\langle f|$ and $|i\rangle$). The simpler approach with fewer approximations can be attributed to the states being investigated. In low loss EELS, both the initial and final states depend heavily on the band structure whereas for core losses the initial states are relatively constant and well defined [40]. Cross section methods however still suffer from the limitations of a one particle final state rule approach and their lack of ability to deal with excitonic effects.

2.3.3   Beth Salpeter Equations -BSE

The largest drawback of TDDFT and cross section calculations is the single particle formalism, which prevents proper treatment of excitonic effects. Solving the BSE is a two particle method that rigorously calculates the interaction between the excited electron and the resulting hole in the core state [42]. It is applicable to both low and core loss EELS calculations [38]. The core of the BSE is in solving the eigenvalue problem involving the effective two particle Hamiltonian [43]:

$$\hat{H}_{\text{eff}} |A_\lambda\rangle = E_\lambda |A_\lambda\rangle \tag{2.32}$$

The effective Hamiltonian can be broken into three parts, the diagonal, exchange and

correlation components[43].

The diagonal component which accounts for single particle transitions:

$$H^{(\text{diag})}_{v c \mathbf{k}, v' c' \mathbf{k}'} = (\epsilon_{c\mathbf{k}} - \epsilon_{v\mathbf{k}})\delta_{vv'}\delta_{cc'}\delta_{\mathbf{kk}'} \tag{2.33}$$

The exchange component which accounts for the repulsive interaction between the excited electron and its hole:

$$H^{(\text{x})}_{v c \mathbf{k}, v' c' \mathbf{k}'} = \int d^3\mathbf{r} \int d^3\mathbf{r'} \varphi_{v\mathbf{k}}(\mathbf{r})\varphi^*_{c\mathbf{k}}(\mathbf{r})\bar{v}(\mathbf{r},\mathbf{r'})\varphi^*_{v'\mathbf{k}'}(\mathbf{r'})\varphi_{c'\mathbf{k}'}(\mathbf{r'}) \tag{2.34}$$

Where φ are the single particle states of the hole and electron and $\bar{v}$ is the unscreened Coulomb potential. Thirdly, there is the correlation component accounting for the attractive interaction between hole and electron:

$$H^{(\text{c})}_{v c \mathbf{k}, v' c' \mathbf{k}'} = -\int d^3\mathbf{r} \int d^3\mathbf{r'} \varphi_{v\mathbf{k}}(\mathbf{r})\varphi^*_{c\mathbf{k}}(\mathbf{r})W(\mathbf{r},\mathbf{r'})\varphi^*_{v'\mathbf{k}'}(\mathbf{r'})\varphi_{c'\mathbf{k}'}(\mathbf{r'}) \tag{2.35}$$

Where W is the screened Coulomb potential on the hole. By treating the hole created by the excited electron as a particle, solving the BSE produces vastly superior results to single particle approaches, particularly in those with moderate screening [43]. However, this method is vastly more computationally demanding and can only be performed on the simplest of structures.

2.3.4   Core Hole Approximation

The computational cost of the BSE method and the difficulties in handling excitonic effects in the single particle approaches has resulted in further approximations being made to improve single particle results. The most prevalent of these is the core hole approximation. This approximation is centred on artificially exciting a DFT into an excited one in order to better calculate the final states in EELS, $\langle f|$. Early implementations involved replacing the excited atom with the next element on the periodic table, called the Z+1 approach [44]. This method was mildly successful, however it lacks the flexibility to handle excitations from different shells, and has since been largely replaced with the core hole approximation [40].

This method involves manually decreasing the occupancy of an excited state, and adding the additional charge to the background to conserve electron number [31]. The effectiveness of the approximation however has been mixed. In some cases, including a core hole results in excellent agreement with experiment, whilst in others, ignoring a core hole produces more accurate results. There have been a number of offered explanations based on the nature of the material: metals tend to not require a core hole due to the increased screening from valence electrons. In general however, spectra tend to fall in between the two extremes, which has led to some *ad hoc* approaches of including non integer core holes, so as to best fit experiment, see Fig 2.12 [40; 45; 46]. This state of affairs has remained unchanged for the past 30 years and consistently leads to unsatisfying results [47–58]. The focus of this work is to improve on this method by developing a first principles method of introducing non-integer core holes. This will then provide the flexibility needed to treat core hole screening in the single particle approach without sacrificing physicality of the results.
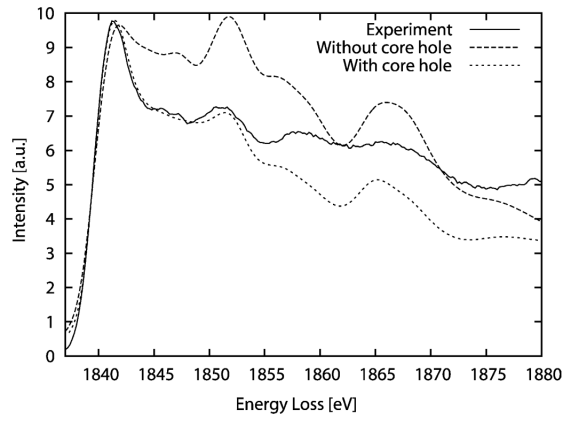
(a)
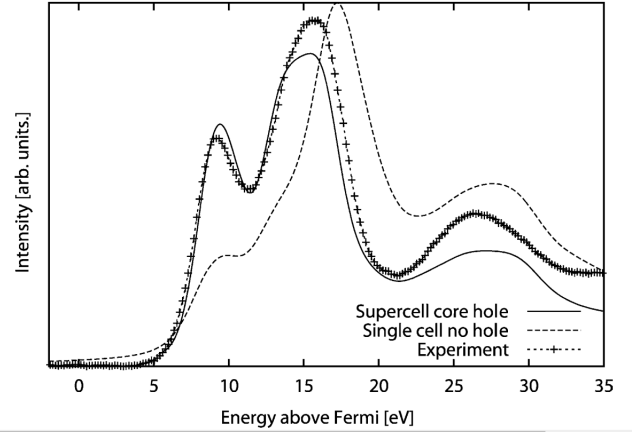
(b)
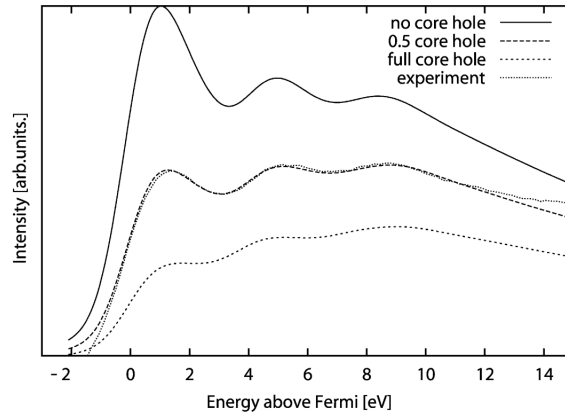
(c)

Figure 2.12: The 3 typical results on core hole on calculations, in 2.12a introducing a core hole results in good agreement with experiment. In 2.12b and 2.12c, the core hole overestimates the excitonic effects resulting in errors in peak intensity. In 2.12c, an *ad hoc* fractional core hole is inserted resulting in good agreement at the cost of physicality.

Chapter 3

Shielding Calculations

The lack of flexibility and accuracy of the core hole approximation combined with the computational deterrent of more exact methods presents a barrier to expanding EELS calculations. Due to their small atomic number, lithium materials are particularly susceptible to these effects as their core states are all low lying. At the same time however, the few electrons involved with lithium help simplify the issue and thus make it an optimum target for improved methods. In this work, a means to extend these barriers was developed by creating a means to perform a first order calculation of shielding effects from the electron density. In this chapter we discuss the formulation and motivation behind this method.

3.1 Core Hole Shielding Calculations

Our goal is to focus on the ionization edges of lithium, with the aim of technique that can be generalized to all elements. To this end, we use the cross section approach under the relativistic single particle approach using the final state rule (FSR), Eq. 2.30[59]:

$$\frac{\partial^2 \sigma}{\partial \Omega \partial E} = \left[\frac{4\gamma^2}{a_0^2 q^4}\right] \frac{k_f}{k_i} \sum_{i,f} |\langle f|e^{i\mathbf{q}\cdot\mathbf{r}}|i\rangle|^2 \delta(E - E_f + E_i) \tag{3.1}$$

As mentioned in Section 2.3.4, shielding effects are contained in the $\langle f|$ term. These effects originate from changes in the Hamiltonian caused by introducing a core hole and

manifest themselves when solving for $\langle f|$ in the Kohn Sham equations (Eq. 2.16) [60]:

$$\left[T_i + V_{\text{ext}}(\mathbf{r}) + V_{\text{H}}(\mathbf{r}) + V_{\text{XC}}(\mathbf{r})\right]\phi_i(\mathbf{r}) = \epsilon_i\phi_i(\mathbf{r}) \tag{3.2}$$

The core hole alters the Hartree and the exchange and correlation potentials, and this effect is reduced somewhat by shielding. The total change in the potential due to introduction of a core hole can be expressed as:

$$\Delta V_{\text{tot}}(\mathbf{r}) = \Delta V_{\text{H}}(\mathbf{r}) + \Delta V_{\text{XC}}(\mathbf{r}) = V_{\text{CH}}(\mathbf{r}) - V_{\text{S}}(\mathbf{r}) \tag{3.3}$$

where $V_{\text{CH}}(\mathbf{r})$ is the potential of a core hole and $V_{\text{S}}(\mathbf{r})$ represents the shielding potential. The current convention in literature when performing core hole calculations is to ignore this shielding term, despite the large effects it has been shown to have on ELNES. We can break the shielding potential into two parts, core electron and valence electron shielding, $V_{\text{c}}(\mathbf{r})$ and $V_{\text{v}}(\mathbf{r})$. Core shielding is due to electrons occupying core orbitals on the excited atom reducing how much the core hole can be "felt" outside of the atom. Valence screening is caused by valence and interstitial electrons being attracted to the positively charged hole. Neither of these terms are readily solvable for using current methods. At this point, an advantage of lithium's low atomic number becomes clear: as there is only one core electron that could shield the hole, we can assume that core electron screening is negligible, which simplifies this problem considerably.

In order to calculate the valence screening we turn to linear response theory, as $\Delta V_{\text{H}}(\mathbf{r})$ and $\Delta V_{\text{XC}}(\mathbf{r})$ cannot be computed exactly. We begin by considering the change in electron density resulting from the introduction of a core hole, as described by Shirley, Soininen and Rehr [61]:

$$\Delta n(\mathbf{r}) = \int d^3\mathbf{r'}\chi^0(\mathbf{r}, \mathbf{r'}; \omega = 0)\Delta V_{\text{tot}}(\mathbf{r'}) \tag{3.4}$$

Where χ^0 is the irreducible polarization function, given by $\chi^0(\mathbf{r}) = \delta n(\mathbf{r})/\delta V(\mathbf{r})$. At this point, we will proceed in assuming no screening ($V_{\text{S}}(\mathbf{r}) = 0$) and then reintroduce in the form of a perturbation. We also restrict our view to only the excited atom, which in this

case gives:

$$\Delta n_{\text{basin}} = \int_f d^3\mathbf{r} n_f(\mathbf{r}) - \int_i d^3\mathbf{r} n_i(\mathbf{r}) = -1 \qquad (3.5)$$

Where the basin defining the integration limits is defined by Bader theory as described in Section 2.2.4. This equation indicates that, when there is no screening, the excited core electron has entirely left the basin, with no response from the material. If we now assume that the polarization is constant inside this basin, we can calculate it as:

$$\frac{\Delta n_{\text{basin}}}{V_{\text{CH}}} = \chi^0_{\text{basin}} = \frac{\Delta n_{\text{basin}}}{\Delta V_{\text{tot}}} \qquad (3.6)$$

If we further assume that the polarization is constant through changes in shielding potential, we can reintroduce the shielding term and perturb the right hand side of Eq. 3.6 to obtain:

$$\frac{-1}{V_{\text{CH}}} = \frac{-1 + \delta n_{\text{basin}}}{V_{\text{CH}} - \delta V_{\text{v}}} \qquad (3.7)$$

Which can be reduced to:

$$\frac{\delta V_{\text{v}}}{V_{\text{CH}}} = \delta n_{\text{basin}} \qquad (3.8)$$

This equation allows connects the screening due to valence electrons to a change in electron density, a rapidly calculable quantity. The screening potential is given in "units" of the core hole potential which allow the screening to be accounted for by modulating the occupancy of the core hole state. Additionally, while we perturbed from the no screening case in Eq 3.7, it should be noted that this argument holds when approached from the full screening case. This indicates that these approximations should hold over the entire range of screening cases ($\delta V_{\text{v}} = 0 \rightarrow V_{\text{CH}}$). We will now discuss how this theory can be implemented into EELS calculations.

3.2   Implementation

Having determined a means of calculating the core hole shielding effects, we describe how these were implemented into ELNES calculations. We begin by performing a standard DFT

calculation with no core hole, followed by one including a full core hole. Depending on cell size, the full core hole calculation is performed using a supercell so as to isolate individual core holes in the periodic boundaries. For both calculations, the electron occupancy inside the lithium atomic basin is calculated and used to calculate the screening potential according to Eq 3.8. This returns a decimal value between 0 and 1 which is subtracted from the magnitude of the hole. A third calculation is then performed with using this non integer "shielded" hole, again using supercells as necessary.

Chapter 4

Applications

Having developed a method and how to implement it, we now apply it to a number of cases of lithium materials. We choose three common lithium compounds with a variety of properties; metallic lithium, ionic LiF, and covalent Li_2O. We also analyze a mixed compound obtained after observing beam damage on LiF during a transformation into metallic lithium, which we will also discuss.

4.1   Lithium Oxide

We begin by investigating Li_2O. The calculations were run on a relaxed cell, converged in terms of K points, and RKmax. Calculations were performed as described in Section 3.2. After the initial two calculations, (with no hole then full hole), the density around the excited lithium atom was plotted, see Fig 4.1. The density plots clearly show valence electrons in the material being attracted to the excited atom. This indicates that the core hole should have both a noticeable effect on the final states and that it is screened as well. We can also see that even the closest lithium atom is largely unaffected by the core hole, in agreement with the supercell size being sufficient to isolate core holes. Calculating the difference in electron occupancy shows a decrease of 0.88 electron in the basin. This decrease is smaller then would be expected the no screening limit and according to Eq 3.8, indicates that the
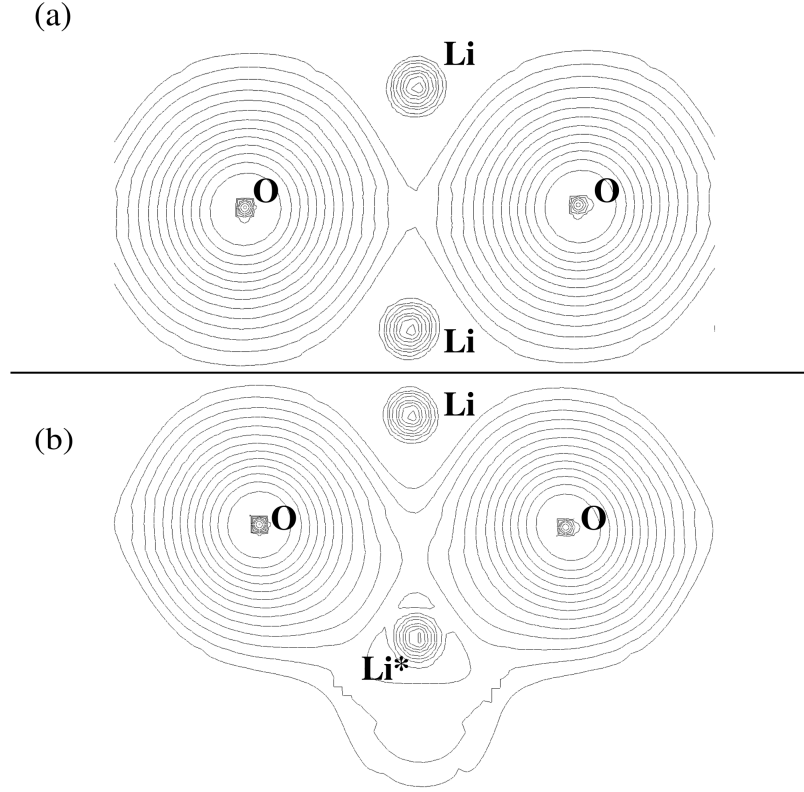
(a)

(b)

Figure 4.1: Effect of introducing a core hole in Li2O. (a) no hole crystal. (b) Crystal with hole on starred lithium atom, inducing a response from the valence electrons. Contour lines on a logarithmic scale.

hole is 12% screened. A third calculation was then performed using a decreased hole size to obtain a final spectra. The ELNES K edge from all three simulations are compared to experiment in Fig 4.2.
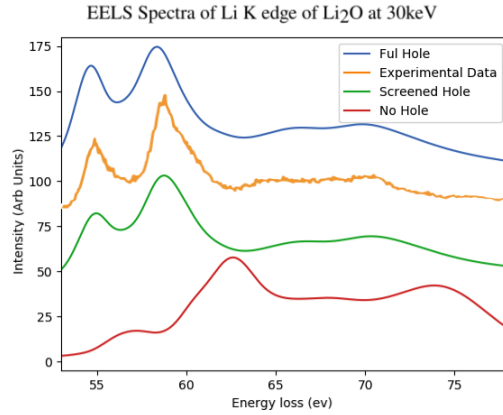
4.2   Lithium

4.3   LiF

Figure 4.2: Lithium K edge of Li_2O from the three calculations taken with varying degrees of core hole.

Bibliography

[1] Vinodkumar Etacheri, Rotem Marom, Ran Elazari, Gregory Salitra, and Doron Aurbach. Challenges in the development of advanced Li-ion batteries: a review. *Energy & Environmental Science*, 4(9):3243–3262, 2011.

[2] B. J. Inkson. Scanning electron microscopy (sem) and transmission electron microscopy (tem) for materials characterization. In Gerhard Hbschen, Iris Altpeter, Ralf Tschuncky, and Hans-Georg Herrmann, editors, *Materials Characterization Using Nondestructive Evaluation (NDE) Methods*, pages 17–43. Woodhead Publishing, 2016.

[3] RF Egerton. Eels in the electron microscope. *Springer, New York p*, 226, 1986.

[4] W. Kohn and L. J. Sham. Self-Consistent Equations Including Exchange and Correlation Effects. *Physical Review*, 140(4A):A1133–A1138, 1965.

[5] Joseph I. Goldstein, Dale E. Newbury, Patrick Echlin, David C. Joy, Charles E. Lyman, Eric Lifshin, Linda Sawyer, and Joseph R. Michael. *Scanning Electron Microscopy and X-ray Microanalysis*. Springer, Boston, MA, 2003.

[6] Michael J. Rust, Mark Bates, and Xiaowei Zhuang. Sub-diffraction-limit imaging by

stochastic optical reconstruction microscopy (storm). *Nature Methods*, 3(10):793–796, 2006.

[7] Eugene Hecht. Optics. *Addison Wesley*, 997:213–214, 1998.

[8] David B. Williams and C. Barry Carter. *Transmission electron microscopy: a textbook for materials science.* Springer, New York, 2nd ed edition, 2008.

[9] Ludwig Reimer. Electron optics of a scanning electron microscope. In *Scanning Electron Microscopy*, Springer Series in Optical Sciences, pages 13–56. Springer, Berlin, Heidelberg, 1998.

[10] Maria Varela, Jaume Gazquez, and Stephen J. Pennycook. Stem-eels imaging of complex oxides and interfaces. *MRS Bulletin*, 37(1):29–35, 2012.

[11] Christian Colliex. An illustrated review of various factors governing the high spatial resolution capabilities in eels microanalysis. *Ultramicroscopy*, 18(1):131–150, 1985.

[12] T. Malis, S. C. Cheng, and R. F. Egerton. Eels log-ratio technique for specimen-thickness measurement in the tem. *Journal of Electron Microscopy Technique*, 8(2):193–200, 1988.

[13] Jaysen Nelayah, Mathieu Kociak, Odile Stphan, F. Javier Garca de Abajo, Marcel Tenc, Luc Henrard, Dario Taverna, Isabel Pastoriza-Santos, Luis M. Liz-Marzn, and Christian Colliex. Mapping surface plasmons on a single metallic nanoparticle. *Nature Physics*, 3(5):348–353, 2007.

[14] Ann-Lenaig Hamon, Jo Verbeeck, Dominique Schryvers, Jan Benedikt, and Richard M. C. M. v d Sanden. Elnes study of carbon k-edge spectra of plasma deposited carbon films. *Journal of Materials Chemistry*, 14(13):2030–2035, 2004.

[15] H. Tenailleau and J. M. Martin. A new background subtraction for low-energy eels core edges. *Journal of Microscopy*, 166(3):297–306, 1992.

[16] A. Gloter, A. Douiri, M. Tenc, and C. Colliex. Improving energy resolution of eels spectra: an alternative to the monochromator solution. *Ultramicroscopy*, 96(3):385–400, 2003.

[17] J. E. Krist. Deconvolution of hubble space telescope images using simulated point spread functions. *Astronomical Data Analysis Software and Systems I, A.S.P. Conference Series*, 25:226–227, 1992.

[18] Frank de Groot. High-resolution x-ray emission and x-ray absorption spectroscopy, 2001.

[19] David S Sholl and Janice A Steckel. *Density functional theory: a practical introduction.* Wiley, Hoboken, N.J., 2009. OCLC: 441874984.

[20] E. K. U. Gross and K. Burke. *Time-Dependent Density Functional Theory.* Lecture Notes in Physics. Springer, Berlin, Heidelberg, 2006.

[21] G. Grff, H. Kalinowsky, and J. Traut. A direct determination of the proton electron mass ratio. *Zeitschrift fr Physik A Atoms and Nuclei*, 297(1):35–39, 1980.

[22] P. Hohenberg and W. Kohn. Inhomogeneous electron gas. *Physical Review*, 136(3B):B864–B871, 1964.

[23] R G Parr. Density Functional Theory. *Annual Review of Physical Chemistry*, 34(1):631–656, 1983.

[24] Jianmin Tao, John P. Perdew, Viktor N. Staroverov, and Gustavo E. Scuseria. Climbing the Density Functional Ladder: Nonempirical Meta–Generalized Gradient Approximation Designed for Molecules and Solids. *Physical Review Letters*, 91(14):146401, 2003.

[25] John P. Perdew, Kieron Burke, and Yue Wang. Generalized gradient approximation for the exchange-correlation hole of a many-electron system. *Physical Review B*, 54(23):16533–16539, 1996.

[26] Axel D. Becke and Erin R. Johnson. A simple effective potential for exchange. *The Journal of Chemical Physics*, 124(22):221101, 2006.

[27] M. J. Frisch et al. Gaussian16 Revision B.01, 2016. Gaussian Inc. Wallingford CT.

[28] David J. Griffiths. *Introduction to quantum mechanics*. Pearson Prentice Hall, Upper Saddle River, NJ, 2005.

[29] Paolo Giannozzi and Baroni. QUANTUM ESPRESSO: a modular and open-source software project for quantum simulations of materials. *Journal of Physics: Condensed Matter*, 21(39):395502, 2009.

[30] Jrgen Hafner. Ab-initio simulations of materials using VASP: Density-functional theory and beyond. *Journal of Computational Chemistry*, 29(13):2044–2078, 2009.

[31] K. Schwarz, P. Blaha, and G. K. H. Madsen. Electronic structure calculations of solids using the WIEN2k package for material sciences. *Computer Physics Communications*, 147(1):71–76, 2002.

[32] V. Mauchamp, F. Boucher, G. Ouvrard, and P. Moreau. Ab initio simulation of the electron energy-loss near-edge structures at the lik edge in li, li2o, and limn2o4. *Physical Review B*, 74(11):115106, 2006. WOS:000240872300038.

[33] Richard F. W. Bader. Atoms in Molecules. In *Encyclopedia of Computational Chemistry*. American Cancer Society, 2002.

[34] Richard F. W. Bader. A quantum theory of molecular structure and its applications. *Chemical Reviews*, 91(5):893–928, 1991.

[35] A. Otero-de-la Roza, Erin R. Johnson, and Vctor Luaa. Critic2: A program for real-space analysis of quantum chemical interactions in solids. *Computer Physics Communications*, 185(3):1007–1018, 2014.

[36] Claudia Ambrosch-Draxl and Jorge O. Sofo. Linear optical properties of solids within the full-potential linearized augmented planewave method. *Computer Physics Communications*, 175(1):1–14, 2006.

[37] Stephen L. Adler. Quantum Theory of the Dielectric Constant in Real Solids. *Physical Review*, 126:413–420, 1962.

[38] Andris Gulans, Stefan Kontur, Christian Meisenbichler, Dmitrii Nabok, Pasquale Pavone, Santiago Rigamonti, Stephan Sagmeister, Ute Werner, and Claudia Draxl. exciting: a full-potential all-electron package implementing density-functional theory and many-body perturbation theory. *Journal of Physics: Condensed Matter*, 26(36):363202, 2014.

[39] V. Mauchamp, P. Moreau, G. Ouvrard, and F. Boucher. Local field effects at Li K edges in electron energy-loss spectra of Li, ${\mathrm{Li}}_{2}\mathrm{O}$ and LiF. *Physical Review B*, 77(4):045117, January 2008.

[40] C. Hebert. Practical aspects of running the WIEN2k code for electron spectroscopy. *Micron*, 38(1):12–28, 2007. WOS:000241994700002.

[41] A. L. Ankudinov, B. Ravel, J. J. Rehr, and S. D. Conradson. Real-space multiple-scattering calculation and interpretation of x-ray-absorption near-edge structure. *Physical Review B*, 58(12):7565–7576, 1998.

[42] E. E. Salpeter and H. A. Bethe. A Relativistic Equation for Bound-State Problems. *Physical Review*, 84(6):1232–1242, 1951.

[43] Stephan Sagmeister and Claudia Ambrosch-Draxl. Time-dependent density functional theory versus BetheSalpeter equation: an all-electron study. *Physical Chemistry Chemical Physics*, 11(22):4451–4457, 2009.

[44] P. A. Lee and G. Beni. New method for the calculation of atomic phase shifts: Appli-

cation to extended x-ray absorption fine structure (EXAFS) in molecules and crystals. *Physical Review B*, 15(6):2862–2883, 1977.

[45] J. Luitz, M. Maier, C. Hbert, P. Schattschneider, P. Blaha, K. Schwarz, and B. Jouffrey. Partial core hole screening in the Cu L3 edge. *The European Physical Journal B*, 21(3):363–367, 2001.

[46] C. Hebert, J. Luitz, and P. Schattschneider. Improvement of energy loss near edge structure calculation using Wien2k. *Micron*, 34(3-5):219–225, 2003. WOS:000184846600012.

[47] R. Brydson, J. Bruley, and J. M. Thomas. Further evidence for core-hole effects in the near-edge structures of light-element K-edges. *Chemical Physics Letters*, 149(4):343–347, 1988.

[48] T. P. Hardcastle, C. R. Seabourne, D. M. Kepaptsoglou, T. Susi, R. J. Nicholls, R. M. D. Brydson, A. J. Scott, and Q. M. Ramasse. Robust theoretical modelling of core ionisation edges for quantitative electron energy loss spectroscopy of B- and N-doped graphene. *Journal of Physics: Condensed Matter*, 29(22):225303, 2017.

[49] E. W. Tait, L. E. Ratcliff, M. C. Payne, P. D. Haynes, and N. D. M. Hine. Simulation of electron energy loss spectra of nanomaterials with linear-scaling density functional theory. *Journal of Physics: Condensed Matter*, 28(19):195202, 2016.

[50] P. Jegadeesan, S. Amirthapandian, Gurpreet Kaur, Sharat Chandra, and B. K. Panigrahi. Characterization of MO bonds in Y2ti2o7 and Y2tio5 with EELS. *physica status solidi (b)*, 252(1):206–211, 2015.

[51] Damien Magne, Vincent Mauchamp, Stphane Clrier, Patrick Chartier, and Thierry Cabioc'h. Site-projected electronic structure of two-dimensional Ti 3 C 2 MXene: the role of the surface functionalization groups. *Physical Chemistry Chemical Physics*, 18(45):30946–30953, 2016.

[52] P. Agrawal, J. Guo, P. Yu, C. Hbert, D. Passerone, R. Erni, and M. D. Rossell. Strain-driven oxygen deficiency in multiferroic ${\mathrm{SrMnO}}_{3}$ thin films. *Physical Review B*, 94(10):104101, September 2016.

[53] Kota Tomita, Tomohiro Miyata, Weine Olovsson, and Teruyasu Mizoguchi. Strong excitonic interactions in the oxygen K-edge of perovskite oxides. *Ultramicroscopy*, 178:105–111, July 2017.

[54] Nicholas L. McDougall, Rebecca J. Nicholls, Jim G. Partridge, and Dougal G. McCulloch. The Near Edge Structure of Hexagonal Boron Nitride. *Microscopy and Microanalysis*, 20(4):1053–1059, August 2014.

[55] Tomohiro Miyata and Teruyasu Mizoguchi. Fabrication of thin TEM sample of ionic liquid for high-resolution ELNES measurements. *Ultramicroscopy*, 178:81–87, July 2017.

[56] Robert F. Klie, Haibin Su, Yimei Zhu, James W. Davenport, Juan-Carlos Idrobo, Nigel D. Browning, and Peter D. Nellist. Measuring the hole-state anisotropy in ${\mathrm{MgB}}_{2}$ by electron energy-loss spectroscopy. *Physical Review B*, 67(14):144508, April 2003.

[57] Stefan Nufer, Thomas Gemming, Christian Elssser, Sibylle Kstlmeier, and Manfred Rhle. Core-hole effect in the ELNES of -Al2o3: experiment and theory. *Ultramicroscopy*, 86(3):339–342, February 2001.

[58] Shang-Peng Gao, Chris J. Pickard, Alexander Perlov, and Victor Milman. Core-level spectroscopy calculation and the plane wave pseudopotential method. *Journal of Physics: Condensed Matter*, 21(10):104203, 2009.

[59] Kevin Jorissen. *The ab initio calculation of relativistic electron energy loss spectra*. PhD thesis, University of Antwerp, 2007.

[60] W. Kohn and L. J. Sham. Self-Consistent Equations Including Exchange and Correlation Effects. *Physical Review*, 140(4A):A1133–A1138, 1965.

[61] E. L. Shirley, J. A. Soininen, and J. J. Rehr. Modeling core-hole screening in core-excitation spectroscopies. *Physica Scripta*, 2005(T115):31, 2005.